CHEMISTRY OF MATERIALS

Article

pubs.acs.org/cm

Designing High-Capacity, Lithium-Ion Cathodes Using X-ray Absorption Spectroscopy

Jason R. Croy,[†] Mahalingam Balasubramanian,*[,‡] Donghan Kim,[†] Sun-Ho Kang,[†] and Michael M. Thackeray*[,†]

[†]Electrochemical Energy Storage Department, Chemical Sciences and Engineering Division, [‡]X-ray Science Division, Advanced Photon Source, Argonne National Laboratory, Argonne, Illinois, 60439

ABSTRACT: We have taken advantage of the element specific nature of X-ray absorption spectroscopy to elucidate the chemical and structural details of a surface treatment intended for the protection of high-capacity cathode materials. Electrochemical data have shown that surface treatments of $0.5Li_2MnO_3 \bullet 0.5LiCoO_2$ ($Li_{1.2}Mn_{0.4}Co_{0.4}O_2$) with an acidic solution of lithium–nickel-phosphate significantly improves electrode capacity, rate, and cycling stability. XAS data reveal that the surface treatment results in a modification of the composite structure itself, where Ni^{2+} cations, intended to be present in a lithium–nickel-phosphate coating, have instead displaced lithium in the transition metal layers of Li_2MnO_3-like domains within the $0.5Li_2MnO_3 \bullet 0.5LiCoO_2$ structure. X-ray diffraction data show the presence of Li_3PO_4, suggesting that phosphate ions from the acidic solution are responsible for lithium extraction and nickel insertion with the formation of vacancies and/or manganese reduction for charge compensation. Furthermore, we show that the above effects are not limited to lithium–nickel-phosphate treatments. The studies described are consistent with a novel approach for synthesizing and tailoring the structures of high-capacity cathode materials whereby a Li_2MnO_3 framework is used as a precursor for synthesizing a wide variety of composite metal oxide insertion electrodes for Li-ion battery applications.

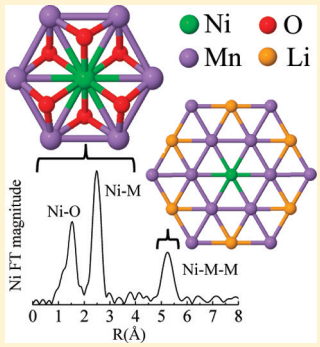

KEYWORDS: *EXAFS, XANES, lithium-ion batteries, composite, cathode, lithium–nickel-phosphate, Li_2MnO_3*

INTRODUCTION

Lithium–metal-oxides remain the most promising cathode materials for high-energy-density lithium-ion batteries for plug-in hybrid electric vehicles (PHEV) and all-electric vehicles (EVs).[1,2] To this end, much effort has been invested to advance these materials. However, a significant challenge that remains is the mitigation of irreversible surface damage at high potentials, which occurs with adverse consequences to the power delivery of the cathodes (i.e., rate capability). To date, several surface passivation techniques have been studied with the goal of addressing this issue in a variety of cathodes by way of 1) enhancing the conductive properties of the surface, 2) modifying the electrode surface chemistry to improve performance, and 3) providing a physical barrier which impedes reactions of the surface with the electrolyte.[3] For example, lithium phosphate/iron-oxide-coated $LiFePO_4$ has been reported to show enhanced rate capability by increasing lithium diffusion at the surface,[4] although the surface character of this material is poorly understood.[5] Surface modification with oxides such as Al_2O_3, MgO, CeO_2, and SnO_2 as well as phosphates have also shown promise for enhancing electrochemical properties of various cathode materials (see ref 6 and references therein). In particular, the resulting surface layer of $AlPO_4$-coated $LiCoO_2$ has been characterized, which shows the absence of $AlPO_4$, possible incorporation of Al into the $LiCoO_2$ structure, and the formation of Li_3PO_4.[7−9] That said, an atomic scale understanding of the structure of these surface-modified materials, and the exact role of surface dopants with respect to electrochemical properties, has not yet been ascertained for many other systems. Furthermore, the proposed mechanisms responsible for electrochemical improvements of treated materials vary widely.[9] Therefore, advances in rational design of new materials is somewhat hindered.

For layered lithium- and manganese-rich metal oxide electrode materials, charge ordering results in preferential arrangements of $LiMn_6$ units in the transition metal layers of the oxide structures.[10] This often bestows Li_2MnO_3-like and $LiMO_2$-like character to small (<5 nm), integrated domains,[11−13] and other interesting ordering schemes.[14−17] This intimate integration of two layered components lends them the classification of composite, "layered–layered" lithium–metal-oxides. As such, they are often written in two-component notation as $xLi_2MnO_3 \bullet (1\text{-}x)LiMO_2$ (M = Mn, Cr, Co, Ni).[18] The Li_2MnO_3 component is significant because it can lend structural stability and provide additional capacity to the electrode if electrochemically activated above 4.5 V. However, the activation process results in 1) a net loss of Li_2O, which damages the surface, and 2) a high, first-cycle, irreversible capacity loss.[19−21] Several strategies have been employed with some success to protect/modify the surface of these cathodes, yet little is known about the effects (i.e., structural, chemical) of such treatments at an atomic scale. Composite, layered–layered

Received: September 7, 2011
Revised: November 7, 2011
Published: November 15, 2011

   dx.doi.org/10.1021/cm2026703 | *Chem. Mater.* 2011, 23, 5415–5424

Table 1. Ni and Co K-Edge EXAFS Parameters[a]

sample	correlation	CN	R (Å)	σ^2 (10^{-4} Å^2)	ΔE (eV)	χ_r^2	k-range (Å^{-1})	R-range (Å)
point 1 (no charge)	Ni−O	6 (set)	2.034 (8)	46 (7)	2.6 (1.2)	26.1	3−14	1.1−3.1
	Ni−M	5.9 (8)	2.874 (6)	39 (8)				
point 2 (4.3 V)	Ni−O short	5.1 (3)	1.903 (5)	32 (6)	2.1 (1.0)	9.7	3−14	1.0−3.1
	Ni−O long	0.9 (3)	2.131 (38)	32 (6)				
	Ni−M	6 (set)	2.857 (5)	38 (3)				
point 3 (4.6 V)	Ni−O short	4.6 (4)	1.893 (9)	35 (11)	3.1 (1.5)	27.3	3−14	1.1−3.1
	Ni−O long	1.4 (4)	2.074 (34)	35 (11)				
	Ni−M	6 (set)	2.860 (9)	61 (5)				
point 4 (2.0 V)	Ni−O	6 (set)	2.027 (8)	45 (6)	3.6 (1.3)	40.3	3−12	1.2−3.2
	Ni−M	6 (set)	2.884 (7)	50 (4)				
Co-LMNO/LCP	Co−O	5.5 (2)	1.919 (8)	23 (3)	1.8 (4)	3.7	2.7−11.8	1.1−3.4
	Co_O−M_O	5.9 (3)	2.864 (39)	60 (4)				
	Co_T−M_O	2.5 (2)	3.377 (60)	60 (4)				
Ni-LCMO/LNP_LT	Ni−O	6.1 (6)	2.045 (5)	53 (9)	1.4 (9)	6.7	2.5−10.5	1.1−3.1
	Ni−P	4.1(1.0)	3.235 (10)	62 (23)				

[a]Possible oxygen loss for highly charged samples was not explicitly considered in the fits. The estimated uncertainties in the last digit(s) of fitted parameters are provided in parentheses.

lithium−metal-oxide materials, in general, have highly complex structures.[22] As such, when dopant levels of an element, meant for surface stabilization/modification, are added to the overall structure, determining relationships between structure and bulk electrochemistry is a daunting challenge. The goal of the present work is to bridge the current gap in scale, and characterize, at the atomic level, the chemical and structural modifications brought about by surface treatments of high-capacity cathode materials.

With these considerations in mind, we have designed an experiment around the unique capabilities of X-ray absorption spectroscopy (XAS). XAS is a powerful tool that provides information on a very local scale (<1 nm) and is well-suited for the characterization of dilute constituents. More importantly, since the interaction of X-rays with any given atomic species (i.e., absorption) is an energy-dependent phenomenon, XAS allows us to probe the local environment of the selected element of interest only. Although XAS is often symbiotically tied to other probes such as X-ray diffraction (XRD), electron microscopy, and pair distribution function (PDF) analysis, it is the element-specific characteristic of XAS, directly giving both chemical and structural information, which differentiates it from other techniques. Furthermore, the ability to determine the electronic and atomic structural details, even for dopant-level constituents, provides a window to study the electronic and structural details of surface treatments that cannot be obtained by conventional diffraction or PDF methods. In this respect, XAS is a unique tool with which the information described herein may be obtained.

For this work, we have chosen a dilute (5 mol %) surface treatment of lithium−nickel-phosphate (Li:Ni:PO_4 ratio = 1:1:1) deposited on a $0.5Li_2MnO_3•0.5LiCoO_2$ ($Li_{1.2}Mn_{0.4}Co_{0.4}O_2$) cathode material. Similar treatments have previously been reported by Kang and Thackeray[23] to enhance electrochemical performance. However, exact structural determinations could not be made regarding the outcome of the surface treatment because the host material was itself a nickel-containing oxide, $0.5Li_2MnO_3•0.5LiNi_{0.44}Co_{0.25}Mn_{0.31}O_2$ ($Li_{1.2}Mn_{0.52}Ni_{0.18}Co_{0.1}O_2$). In the present case, the host material was chosen to be free of nickel ($0.5Li_2MnO_3•0.5LiCoO_2$), and, therefore, structural and chemical information obtained from XAS measurements provide direct information about electrochemical enhancements due to the Li−Ni−PO_4 treatment itself relative to untreated electrodes. Our findings have exciting implications for tailoring the structures and/or surfaces of high-capacity composite electrodes derived from a Li_2MnO_3 precursor and improving their structural stability over long-term cycling.[24]

EXPERIMENTAL SECTION

Synthesis of $0.5Li_2MnO_3•0.5LiCoO_2$/Li−Ni−PO_4. A $(Co_{0.5}Mn_{0.5})CO_3$ precursor was prepared by mixing a 0.1 M solution of cobalt sulfate and manganese sulfate with a 0.5 M solution of ammonium bicarbonate. The final solution was stirred overnight, filtered, dried, and then lightly ground. A $0.5Li_2MnO_3•0.5LiCoO_2$ sample, hereafter referred to as LCMO, was prepared by thoroughly mixing stoichiometric amounts of the $(Co_{0.5}Mn_{0.5})CO_3$ precursor and Li_2CO_3 followed by annealing in air at 550 °C for 24 h. The mixture was allowed to cool, lightly ground, and annealed again in air at 850 °C for an additional 12 h. The final powder was again ground and sieved (<150 μm). The sample was then surface-treated with lithium−nickel-phosphate [Li:Ni:PO_4 = 1:1:1 (LNP)] using an acidic sol−gel method as previously reported,[23] which includes drying at ∼100 °C and subsequent annealing at 550 °C. A sample of the dried only powder (∼100 °C) was also taken and pressed into a pellet for XAS comparison with its fully annealed (550 °C) counterpart. In addition, a second, coated sample was prepared in similar fashion by treating $0.5Li_2MnO_3•0.5LiMn_{0.5}Ni_{0.5}O_2$ (LMNO) with lithium−cobalt-phosphate [Li:Co:PO_4 = 1:1:1 (LCP)]. X-ray diffraction patterns (XRD) of the powder samples were collected on a Siemens D5000 diffractometer between 10 and 80° 2θ using CuKα radiation.

Electrochemical Cells. Cathodes and electrochemical cells were prepared by standard procedures, the details of which have been reported elsewhere.[24] Three cells with LNP-treated cathodes were brought to predetermined states of charge on the first charge/discharge cycle (4.6−2.0 V, 15 mA/g) and opened in an argon-filled glovebox where the cathodes were removed and then sealed in thin, aluminum-coated pouches. These pouch-cells as well as reference samples were used for the X-ray absorption experiments.

X-ray Absorption Spectroscopy. XAS experiments were carried out at beamline 20-BM-B of the Advanced Photon Source at Argonne National Laboratory, IL. The incident beam was monochromatized using a Si(111) fixed-exit, double-crystal monochromator. In all cases, a Mn, Co, or Ni foil was incorporated, as appropriate, for energy calibration with the zero energy (E_0) defined according to Kraft et al.[25] Harmonic rejection was facilitated by the use of a Rh-coated mirror as well as a 20% detuning of the beam intensity at ∼400 eV above the edge of interest. Mn K- and Co K-edge spectra of the treated and

dx.doi.org/10.1021/cm2026703 | Chem. Mater. 2011, 23, 5415−5424

untreated LCMO electrodes were acquired in transmission mode utilizing gas ionization chambers as detectors. Ni K-edge data of LNP-treated LCMO samples and Co K-edge data of LCP-treated LMNO samples were acquired in the fluorescence geometry using an energy discriminating, multielement, Ge detector.

X-ray Absorption Near Edge Structure (XANES) and Extended X-ray Absorption Fine Structure (EXAFS) data were extracted with established methods using the ATHENA software package.[26] The normalized EXAFS was converted from energy to k-space and weighted by k^3. These data were then Fourier transformed to R-space and left uncorrected for photoelectron phase shifts. As such, distances in R-space are ~0.4 Å shorter than actual bond distances. Structural parameters were obtained by fitting within the ARTEMIS software package which utilizes the IFEFFIT library of XAFS algorithms.[26] The k- and R-ranges for all fits are provided in Table 1.

RESULTS AND DISCUSSION

X-ray Diffraction. Figure 1 shows the XRD patterns of (a) untreated LCMO, (b) LNP-treated LCMO, (c) LCP-treated LMNO, and (d) LCMO treated with LNP at low temperature (~100 °C). Patterns (a)-(c) are typical of structurally integrated, layered structures containing both Li_2MnO_3-like domains as well as $LiMO_2$ (M = Co, Ni, Mn) components.[10,27] For example, the features between 20° and 23° 2θ are characteristic of $LiMn_6$ cation ordering in the transition metal layers of Li_2MnO_3.[28] Thus, these samples are consistent with reports of small (<5 nm), integrated domains of Li_2MnO_3 and $LiMO_2$ (M = Mn, Co, Ni).[11] However, for the phosphate-treated samples in (b) and (c) we note the appearance of additional, weak reflections in the 20−35° 2θ range (asterisks in Figure 1). These peaks are assigned to the formation of Li_3PO_4, in agreement with Popovic et al.,[29] and are consistent with previous reports of similarly prepared materials.[23] Figure 1(d) shows that treatment of LCMO with the Li−Ni−PO_4 solution and subsequent heating at 100 °C does not produce the same Li_3PO_4 peaks but rather causes an overall suppression of peak intensities and a disappearance of the ordering peaks at ~22° 2θ.

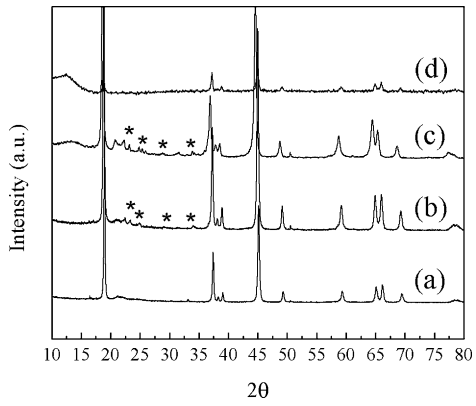

Figure 1. XRD patterns of (a) the LCMO host, (b) LNP-treated LCMO, (c) LCP-treated LMNO, and (d) low-temperature (~100 °C) LNP-treated LCMO. Peaks associated with Li_3PO_4 are indicated (*).

X-ray Absorption Spectroscopy. Figure 2(a) shows an example of an X-ray fluorescence spectrum taken with the multielement Ge detector. Because of the energy discriminating capabilities of the detector, proper choice of energy windows allows one to preferentially count only those fluorescence photons which are generated by the element of interest. For example, the data shown in Figure 2(a) were acquired from the LNP-treated LCMO sample at 10.0 keV. This sample has a relatively small concentration of nickel (5 mol %), making the detection/analysis of the Ni K fluorescence difficult due to the high intensities of the nearby Mn and Co K-peaks. However, setting an energy window which includes contributions mainly from the Ni K_α between ~7250 eV and ~7600 eV [dashed lines, Figure 2(a)] effectively filters the contributions from the more prevalent Mn and Co. Even though the Co K_β peak (~7650 eV) overlaps with the Ni K_α peak (~7480 eV), its share in the overall fluorescence signal can be largely eliminated. Figure 2(b) shows the raw, unnormalized absorption data from the Mn (black), Co (red), and Ni (blue) K-edges, acquired in transmission mode, of the LNP-treated LCMO sample. Note that the small edge jump for the nickel absorbers, relative to manganese and cobalt, is consistent with the expected concentrations of these elements. As shown, the high-energy region of the cobalt data overlaps with the low-energy (pre-edge) region of the nickel data; therefore, Co EXAFS oscillations appear in the Ni absorption transmission data. This is evident in the inset of Figure 2(b) for the normalized transmission pre-edge region of the Ni K-edge (red). However, after the application of the energy window, the oscillations are largely absent in the energy-discriminated,

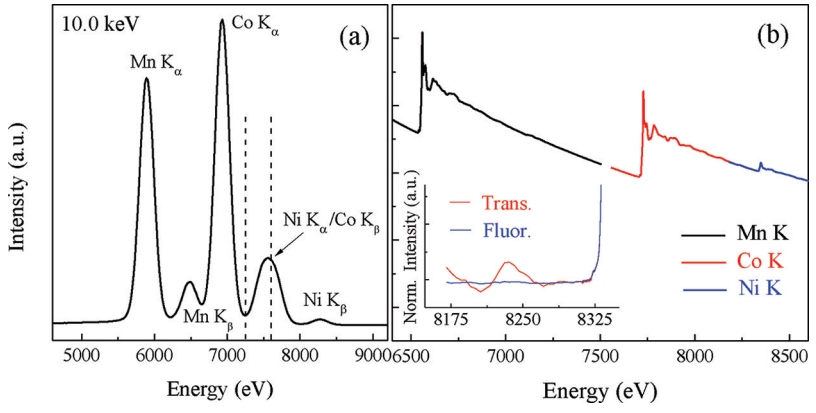

Figure 2. (a) X-ray fluorescence spectrum of LNP-treated LCMO acquired at 10.0 keV with a multielement Ge detector. Dashed lines indicate the window of discrimination used to isolate Ni K_α fluorescence. (b) Raw, unnormalized absorption data from Mn (black), Co (red), and Ni (blue) K-edges, acquired in transmission mode, of LNP-treated LCMO. The inset in (b) shows normalized pre-edge regions of Ni K transmission (red) and energy-filtered fluorescence (blue) data.

dx.doi.org/10.1021/cm2026703 | Chem. Mater. 2011, 23, 5415−5424

normalized fluorescence data (blue), which shows a relatively flat, smooth pre-edge. Thus, we are able to directly analyze the EXAFS of nickel despite its dilute concentration and proximity in energy to cobalt.

Figure 3 shows the first charge/discharge curve between 4.6 and 2.0 V (15 mA/g) for a LNP-treated LCMO electrode. The

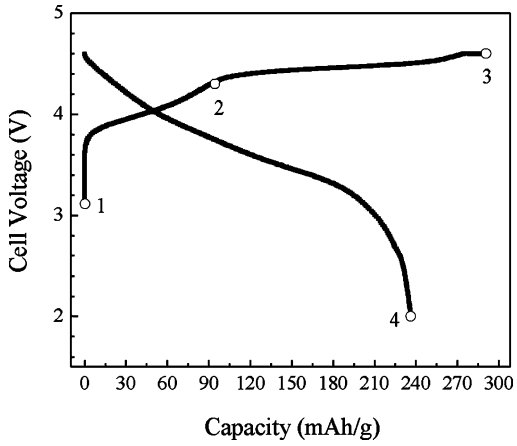

Figure 3. Charge/discharge curve between 4.6 and 2.0 V (15 mA/g) for LNP-treated LCMO electrodes. Numbered points indicate predetermined states of charge at which cells were prepared for XAS measurements.

numbered points along the curves indicate predetermined states of charge at which cells were prepared for the XAS measurements. Point 1 represents the fresh, uncharged electrode, point 2 (at ~4.3 V) corresponds to the extraction of ~90 mAh/g capacity, and point 3 represents a fully charged electrode at 4.6 V corresponding to the full ~280 mAh/g practical capacity of the electrode. Point 4 represents a fully discharged electrode at 2.0 V after one complete cycle.

In general, the results obtained at all points of charge for the Mn (not shown) and Co K-edges agree well with those reported elsewhere for manganese and cobalt in similar systems.[30−34] We therefore focus our attention on the dilute elements of interest; namely, nickel and cobalt as introduced by way of surface treatments on LCMO and LMNO, respectively. However, several observations are worth noting. For example, from the XANES data in Figure 4(a), it can be observed that the cobalt environment in the parent LNP-treated LCMO electrode (point 1, Figure 3) is identical to the Co environment in the untreated LCMO sample; both spectra overlap and are similar to Co^{3+} in $LiCoO_2$, again revealing the composite nature of the material. This observation reveals that the LNP treatment has little effect on the Co-rich regions of the composite material. However, from the Fourier transformed Mn K-edge data in Figure 4(b), in which Li_2MnO_3 is used as a reference, it can be seen that the local environment of manganese in the LNP-treated LCMO has undergone slight modifications with respect to that of manganese in the parent LCMO. Both LCMO and LNP-treated LCMO samples show increased amplitudes in the second-shell Mn−M correlations at ~2.5 Å with respect to pure Li_2MnO_3. For LCMO, this is attributed to contact between the boundaries of the $LiCoO_2$- and Li_2MnO_3-like domains, in agreement with Bareno et al.[11] For LNP-treated LCMO, even higher amplitudes for the Mn−M correlation are observed. This result is attributed to the insertion of nickel into the transition metal layers of the

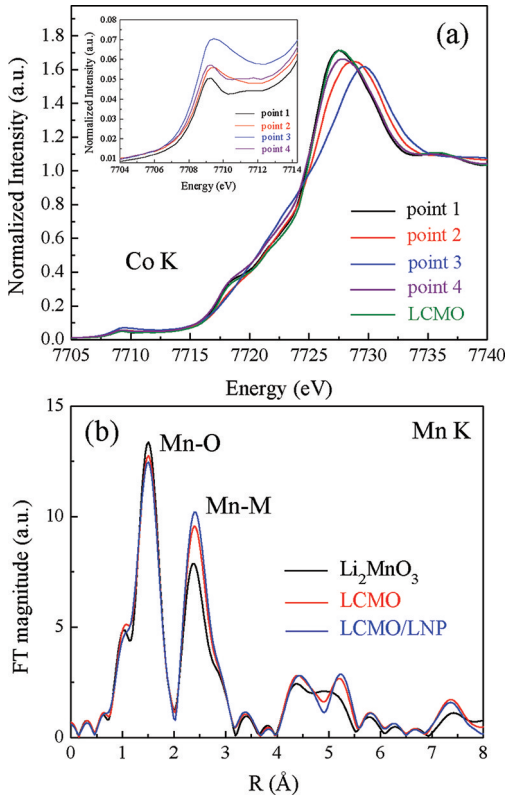

Figure 4. (a) Co K-edge XANES showing LNP-treated LCMO at all points of charge in Figure 3 and untreated LCMO. The inset in (a) shows a magnified view of the Co K pre-edge region for all points of charge. (b) Magnitude of the Fourier transformed Mn K-edge data for LNP-treated LCMO, untreated LCMO, and a Li_2MnO_3 reference.

Li_2MnO_3-like domains in the $0.5Li_2MnO_3 \bullet 0.5LiCoO_2$ composite structure as described in more detail below.

Figure 5(a) shows the Ni K-edge XANES data of the LNP-treated LCMO electrode at points 1 and 4 in the electrochemical data (Figure 3) relative to a Ni^{2+} reference, $0.5Li_2MnO_3 \bullet 0.5LiMn_{0.5}Ni_{0.5}O_2$ (alternatively, $Li_{1.2}Mn_{0.6}Ni_{0.2}O_2$). The excellent overlap of all three spectra indicates that the nickel ions are predominantly divalent in the uncharged electrode as well as after one complete cycle. Figure 5(b) shows the Ni K-edge XANES data of the LNP-treated LCMO electrodes at points 1, 2, and 3 of Figure 3 relative to Ni^{3+} ($LiNi_{0.8}Co_{0.2}O_2$) and Ni^{4+} ($LiNi_{0.8}Co_{0.2}O_2$ charged to 5.2 V) references, as reported by Balasubramanian et al.[16] At a relatively early stage of charge, point 2 (4.3 V), the nickel ions reach an oxidation state of ~3+. This finding is significant because it would be expected that a lithium−nickel-phosphate such as olivine $LiNiPO_4$ (Li:Ni:PO_4 = 1:1:1) should be electrochemically inactive to 5.0 V;[35] the result therefore reveals that the nickel ions partake in the electrochemical reaction. Further charging to point 3 (4.6 V, Figure 3), when the cell is fully charged, apparently does not increase the oxidation of the nickel ions much further, indicating that the average oxidation is still significantly below 4+. This is an intriguing result, because the bulk oxidation process in other layered nickel oxide electrodes often involves the oxidation of nickel to the tetravalent state during high states of charge.[2,34,36,37]

Figure 6(a) shows examples of the raw, isolated EXAFS oscillations (k^3 weighted) above the dopant, Ni K-edge for

dx.doi.org/10.1021/cm2026703 | Chem. Mater. 2011, 23, 5415−5424

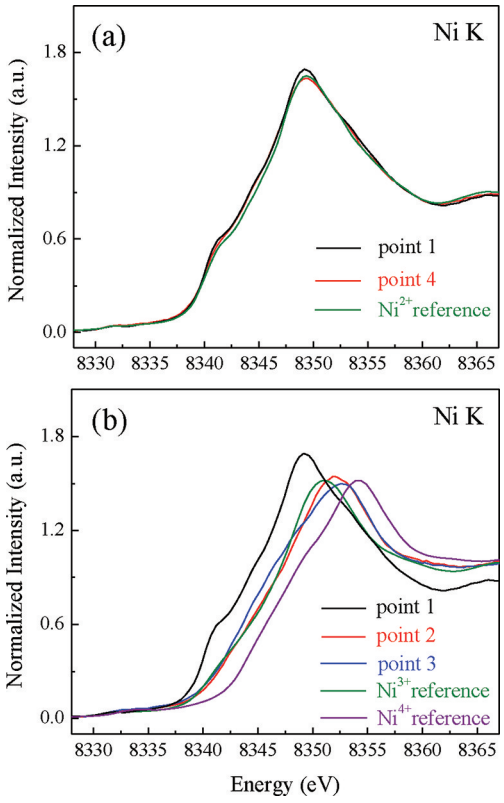

Figure 5. (a) Ni K-edge XANES of LNP-treated LCMO electrodes at charge points 1 and 4 in Figure 3 and a Ni^{2+} reference. (b) Ni K-edge XANES at points 1, 2, and 3 and Ni^{3+} and Ni^{4+} references.

electrodes at points 1 and 2 in the electrochemical data (Figure 3). The data are of high quality, at least up to 15 $Å^{-1}$. Figure 6(b) shows the magnitude of the Fourier transformed k-space data for electrodes at points 1, 2, and 3; the inset compares the data collected at points 1 and 4 (Figure 3). One of the most significant observations that can be made by visual inspection of the transformed data at point 1 is the fact that the nickel in this sample is not present in an olivine-type $LiNiPO_4$ structure. This conclusion is evident from 1) the high amplitude of the Ni−M correlation relative to the Ni−O correlation, indicating a large number of near-neighbor metal atoms, 2) the R value of this peak indicates a bond distance of ~2.87 Å [Figure 6(b) is not corrected for phase shifts)], which is significantly less than the ~3.81 Å expected for Ni−Ni bond distances in $LiNiPO_4$,[38] and 3) the large peak centered at ~5.2 Å indicates three-body, Ni−M−M correlations associated with the nickel environment in this material. Furthermore, the general appearance of the Fourier transform of the EXAFS data is often a powerful "fingerprinting" tool used to decode the local environment of an absorbing element. As such, Figure 6(b) suggests that the local structure of Ni in LNP-treated LCMO electrodes is similar to the local structure of Co in $LiCoO_2$. In such layered structures, the first-shell M−O coordination is 6, as is the second-shell M−M coordination. In addition, a pronounced peak associated with collinear M−M−M correlations within the transition metal plane is also present, similar to the peak in Figure 6(b) at ~5.2 Å. Furthermore, absent from the R-space data of Figure 6(b) is a discernible peak between ~3.5 and ~4.0 Å. Such a peak would reveal 180° Ni−O−Ni correlations that are present when Ni occupies sites within the lithium layers of these layered materials.[39] These observations, in conjunction

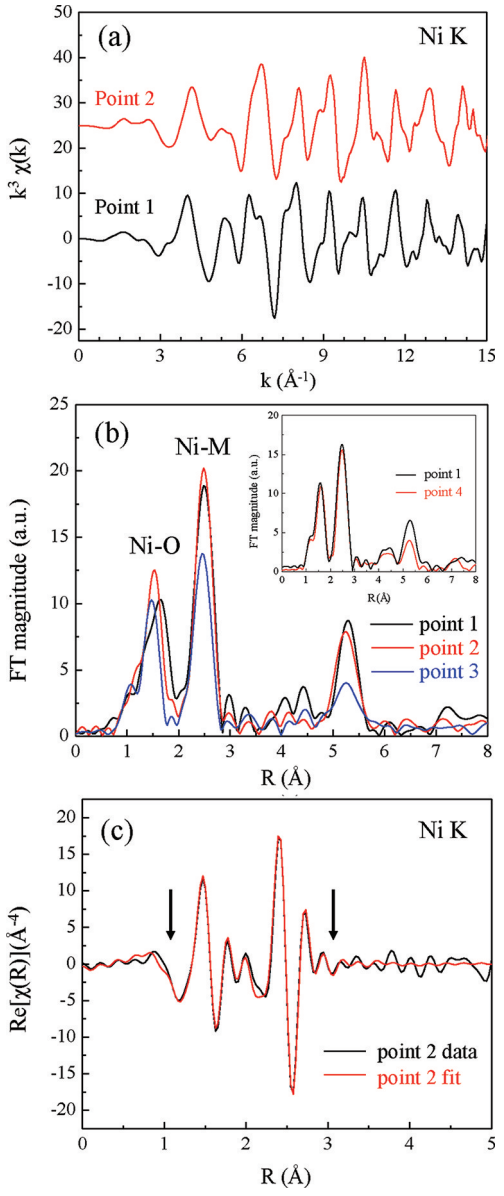

Figure 6. (a) Raw, isolated EXAFS oscillations (k^3 weighted) above the Ni K-edge for electrodes at points 1 and 2 in Figure 3. (b) Magnitude of Fourier transformed data for electrodes at charge points 1, 2, and 3; the inset compares points 1 and 4. (c) Real part of Fourier transformed data for point 2 (4.3 V, black) along with the fit of the first two shells (red) using two different Ni−O bond lengths to account for Jahn−Teller-distorted Ni^{3+}. Arrows indicate the range of the fit.

with the Li_3PO_4-like peaks in the XRD patterns of Figure 1, lead us to conclude that the lithium ions in the transition metal layers of the Li_2MnO_3-like regions have been substituted by nickel, facilitated by phosphate ions during the acidic Li−Ni−PO_4 treatment and subsequent annealing of the parent LCMO. Therefore, the model used for EXAFS analysis is a Li_2MnO_3-type structure in which the nickel ions reside in the lithium (2b) sites of the transition metal layers (Li_2MnO_3 space group: monoclinic, $C2/m$), i.e., the $LiMn_6$ units in the Li_2MnO_3 domains are replaced by $NiMn_6$ units. This model is also consistent with our XANES data that reveal the divalent and tetravalent nature of Ni and Mn, respectively, as is also the case, for example, in $LiMn_{0.5}Ni_{0.5}O_2$.[17] However, for points 2 and 3

dx.doi.org/10.1021/cm2026703 | Chem. Mater. 2011, 23, 5415–5424

on the charge profile (Figure 3), the XANES data in Figure 5(b) reveal that the nickel ions are trivalent. As such, a Jahn–Teller distortion is expected, accompanied by the appearance of differing first-shell, Ni–O bond lengths[16,40–43] with 4 "short" distances of ~1.92 Å and 2 "long" distances of ~2.16 Å (using Cartesian coordinates from the $NaNiO_2$ structure as input). For the fitting of the Ni^{3+} states (points 2 and 3 in Figure 3), the total coordination number of the first shell was constrained to be 6, while the disorder parameter (σ^2) was constrained to be equal for both first-shell Ni–O bonds. One value of ΔE was found to be sufficient for each state of charge. An amplitude reduction factor (S_0^2) of 0.85 for Ni was determined by fitting absorption data from a nickel foil reference.

Table 1 shows the results of a fitting analysis conducted for the first two shells of the Ni K-edge data at points 1–4 [see Figure 6(b)] with errors in parentheses. For the uncharged electrode (point 1), the Ni–O coordination number was set at the model value of 6. From this starting point, a second-shell, Ni–M coordination number of 5.9 (8) was obtained from the fit, consistent with nickel in octahedral (2b) sites surrounded by six manganese ions, giving rise to $NiMn_6$ units in the transition metal layers. Bond distances of ~2.03 Å (Ni–O) and ~2.87 Å (Ni–M) are consistent with the Li_2MnO_3 model values of 2.06 Å (Li–O) and 2.86 Å (Li–M) for the Li atoms in the transition metal layer. Point 1 was also fit assuming a split, first-shell to evaluate the possibility of some Ni^{3+} in the uncharged electrode; however, reasonable fits could only be obtained with unphysical values of the disorder parameter, σ^2. As such, we conclude that the nickel ions in the uncharged electrode are predominantly divalent.

For points 2, 3 ,and 4, the Ni–M coordination number was fixed at 6 as determined by the fit at point 1. Figure 6(c) shows the real part of the transformed data for point 2 (4.3 V, black) along with the fit of the first two shells (red) using two different Ni–O bond lengths. The fit was also performed assuming only one Ni–O bond distance; however, the reduced-chi-squared (χ_r^2) value for this fit was 59.0, compared to a χ_r^2 value of just 9.7 when two Ni–O bond distances were included (Table 1). Coordination numbers of ~5 and ~1 were obtained for the short and long Ni–O bonds, respectively. This implies that when the cell is charged to ~4.3 V, not all the nickel ions are trivalent because the short and long coordination numbers would have been 4 and 2, respectively. However, when Ni^{3+} is oxidized to Ni^{4+}, the ion reverts to a symmetric, undistorted (Jahn–Teller free) configuration with a Ni–O bond distance of ~1.89 Å, i.e., very close to the 1.9 Å of the "short" Ni^{3+}–O bond. Therefore, given the tendency of Ni^{2+} to oxidize to Ni^{4+} in these systems, it is likely that the coordination numbers reveal a combination of Ni^{3+} and Ni^{4+} at this state of charge (point 2). On further charging to 4.6 V (point 3 in Figure 3) the first shell of Ni–O remains split with an increase in the number of "long" bonds (1.4) at the expense of the "short" bonds (4.6). At this state of charge, oxygen loss from the structure is expected and is, in fact, evident from the heavy suppression of the peak at ~5.2 Å that reveals local distortions. For nickel ions close to the surface, oxygen loss likely occurs with a concomitant reduction of Ni^{4+} to Ni^{3+}, thereby increasing the number of Jahn–Teller distorted, "long" bonds as shown in Table 1. We note that the split Ni–O shells at charge points 2 and 3 give further credence to our model of nickel ions occupying sites within the transition metal layers of the Li_2MnO_3-like domains. For example, if nickel were to substitute for cobalt in the $LiCoO_2$ domains, it would reside as Ni^{3+} for charge balance. However, from the XANES data above, it is observed that the nickel oxidation state is predominantly 2+ in the as-prepared electrode (point 1 in Figure 3). In addition, nickel, surrounded by a majority of cobalt atoms as near-neighbors in similar systems, exists as $Ni^{3+}Co^{3+}$ and does not show a Jahn–Teller distortion,[40,41] in contrast to the nickel ions in the LNP-treated LCMO sample. From Table 1, the "long" bond distance of ~2.13 Å is too large to be associated with Ni–O distances in Co-rich ($Ni^{3+}Co^{3+}$) systems in which the Co-oxide host structure is known to dictate Ni^{3+}–O bond distances (~1.89 Å). On discharge to 2.0 V, the first-shell Ni–O bonds are no longer split, and one oxygen distance corresponding to the original structure provides the best fit to the data. However, although the Ni^{2+} to Ni^{3+} oxidation process appears to be reversible, the material undergoes an irreversible structural change as highlighted by the EXAFS data [inset in Figure 6(b)], which compares the nickel correlations in the electrode structure before and after cycling. The difference in the two sets of EXAFS data is attributed to oxygen loss and the associated structural changes that occur on the 4.5 V plateau. The finding that the average oxidation state of the nickel ions is lower than 4+ after significant delithiation is unique compared to related systems where the average oxidation state of the nickel ions is closer to 4+. This observation speaks directly to the importance of understanding the local structural environment of nickel, which can be expected to play a key role in the overall electronic and structural evolution on repeated cycling.

Figure 7(a) shows the Fourier transformed Co K-edge data of the Li–Co–PO_4-treated LMNO sample compared with the untreated and LNP-treated LCMO materials. It is observed in the LCP-treated LMNO sample that cobalt has a significant deficiency of metal neighbors relative to the other two samples. In addition, the amplitude of the Co–O correlation is now stronger than the Co–M correlation. Furthermore, the focusing peak at ~5.2 Å is severely damped, indicating an absence, or increased disorder, of nearly collinear Co–M–M correlations. Clearly, Co does not exist exclusively within a well-defined layered $LiCoO_2$-like structure. Fits to the data using only $LiCoO_2$ as a model did not produce acceptable results. In addition, the olivine structure of $LiCoPO_4$ is similar to that of $LiNiPO_4$[44] and, as seen in the inset of Figure 8(a), bears no resemblance to the Co EXAFS of Figure 7(a). Thus, as for the Li–Ni–PO_4-treated LCMO sample, surface treatment and subsequent annealing of LMNO with Li–Co–PO_4 does not lead to the intended 'Li–Co–PO_4' surface coating. Rather, we argue that cobalt, like nickel, has also been incorporated into the host electrode structure. In this case, if the cobalt ions were to replace Mn^{4+} or Ni^{2+} of the parent LMNO ($Li_{1.2}Mn_{0.6}Ni_{0.2}O_2$) structure, it would have to do so equally to maintain charge balance (e.g., $Mn^{4+}Co^{3+}Ni^{2+}$). This should result in two things. First, because the lithium ions in the transition metal layers of the $Li_{1.2}Mn_{0.6}Ni_{0.2}O_2$ host material tend to charge order with Mn^{4+} ions forming $LiMn_6$ clusters, any cobalt that substitutes for manganese would likely see a decrease in M neighbors from ~6 to ~3, whereas any cobalt that substitutes for nickel would likely maintain a Co–M coordination of ~6 (see, for example, Thackeray et al.[22]). Therefore, the average Co–M correlation should decrease. Second, because the manganese ions in this arrangement are surrounded by lithium ions, the collinear alignment of three metal atoms, giving rise to the "focusing" peak at 5.2 Å, is severely disturbed. From Figure 7(a) we can see evidence of

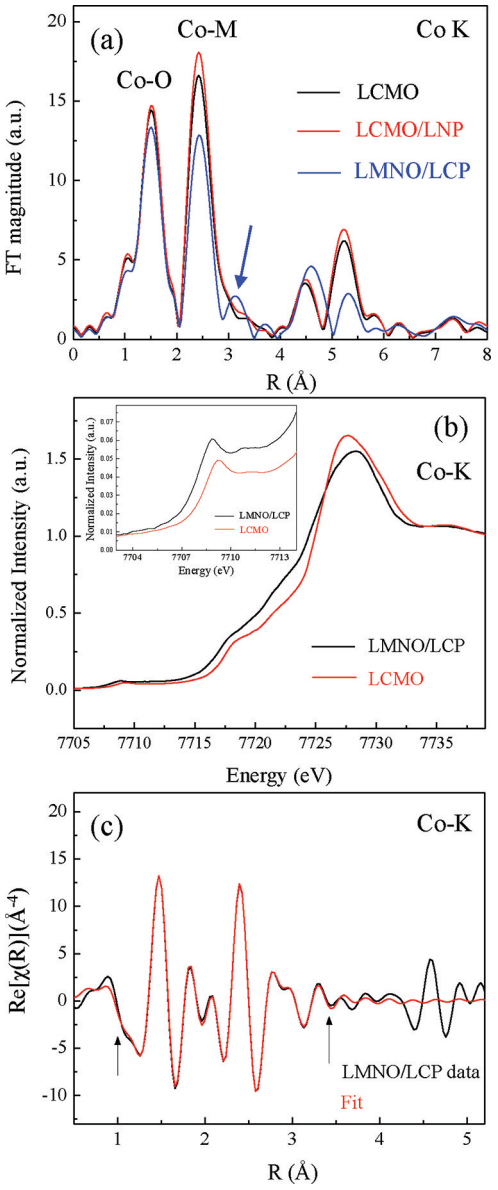

Figure 7. (a) Magnitude of Fourier transformed Co K-edge data of the LCP-treated LMNO compared with untreated- and LNP-treated LCMO. (b) Co K-edge XANES of LCP-treated LMNO and untreated LCMO. The inset in (b) shows a magnified view of the Co K pre-edge region. (c) Real part of Fourier transformed LCP-treated LMNO Co K-edge data (black) along with the fit to the data (red). Arrows indicate the range of the fit.

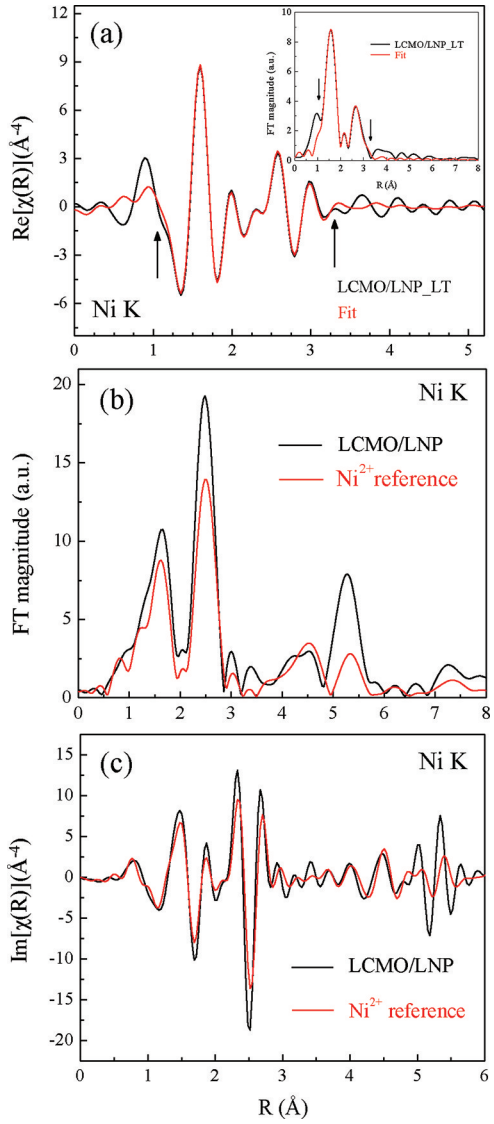

Figure 8. (a) Real part of the Fourier transformed LNP-treated LCMO Ni K-edge data (black) along with the fit to the data (red) using the olivine $LiNiPO_4$ structure as input. Arrows indicate the range of the fit. Data were acquired on a sample treated at low temperature (LT), ~100 °C, after the $LiNiPO_4$ sol–gel process. The inset in (a) shows the corresponding Fourier transform magnitudes. (b) Comparison of Fourier transformed Ni K-edge data (3–13 $Å^{-1}$) of LNP-treated LCMO and Ni^{2+} reference ($0.5Li_2MnO_3 \bullet 0.5LiMn_{0.5}Ni_{0.5}O_2$). (c) Imaginary parts of Fourier transformed Ni K-edge data of LNP-treated LCMO and a Ni^{2+} reference revealing an increasing phase mismatch with increasing R.

these features in the LCP-treated LMNO sample. The Co–M correlation is clearly smaller than what is expected for a $LiCoO_2$-type arrangement (e.g., Co substituting Ni), and the peak at 5.2 Å is heavily suppressed (e.g., Co–Li–M correlations for Co substituting Mn). However, as seen in the Fourier transform of the LCP-treated LMNO of Figure 7(a), a well-resolved peak appears at ~3.1 Å (arrow). This peak is consistent with the occupation of the 6c tetrahedral sites in $LiCoO_2$ (space group = $R3\bar{m}$) by cobalt, which is reminiscent of correlations between cobalt in the tetrahedral and octahedral sites of the Co_3O_4 spinel structure.[45] In addition, Figure 7(b), which shows the Co K-edge XANES data of LCP-treated LMNO and untreated LCMO samples, reveals that the valency of the cobalt ions in the LCP-treated sample is not trivalent but is somewhat reduced toward Co^{2+}. The inset of Figure 7(b) shows that the Co K pre-edge XANES peak of the LCP-treated LMNO sample is significantly stronger relative to that of the untreated LCMO sample, which is also consistent with the noncentrosymmetric environment of tetrahedral, compared to octahedral, cobalt.[46]

Considering the above discussion, fits to the LCP-treated LMNO data of Figure 7(a) were conducted using $LiCoO_2$ as a starting point with some cobalt in the tetrahedral 6c sites using crystallographic data from Gummow et al. for 'low-temperature' $LiCoO_2$ synthesized at 400 °C (LT-$LiCoO_2$).[47] The results are shown in Figure 7(c) and Table 1. One value of ΔE was found to be sufficient for all paths; the disorder parameters (σ^2) for

dx.doi.org/10.1021/cm2026703 | Chem. Mater. 2011, 23, 5415–5424

Co−M correlations, of both octahedral (Co_O−M_O) and tetrahedral (Co_T−M_O) atoms, were constrained to be the same. The coordination number is strongly correlated to σ^2, and the Co_T−M_O coordination number must be viewed with this in mind. However, the EXAFS-derived bond distances are highly accurate and can be used for structural comparisons. An amplitude reduction factor (S_0^2) for cobalt of 0.8 was found by fitting absorption data from a cobalt foil reference. The first-shell, Co−O bond distance of ∼1.92 Å (Table 1) matches that of the expected ∼1.91 Å of Co^{3+}−O in $LiCoO_2$. However, tetrahedrally coordinated, divalent cobalt ions have a Co−O bond distance of ∼1.96 Å,[48] which could not be resolved here. Resolving two different, but similar peaks in EXAFS requires a separation of the peaks by a minimum of $\Delta R \sim \pi/2k_{max}$, k being the photoelectron wavenumber. In this case, k_{max} is 11.8 $Å^{-1}$ making the smallest resolvable peak separation ∼0.14 Å. However, we do find a first-shell, Co−O coordination number of ∼5.5, lower than the expected coordination number of 6 for octahedral cobalt; this result is consistent with the XANES data that shows evidence of some Co^{2+} that likely occupy tetrahedral sites (coordination number = 4). For the Co−M correlations there are clearly two resolvable peaks. From the fit (Table 1), the first peak was observed at ∼2.86 Å and is consistent with the expected M−M distance between M ions in the edge-shared octahedra of these layered structures. The second peak appears at ∼3.38 Å. We ascribe this distance to correlations of cobalt ions occupying tetrahedral sites with other metal ions at regular octahedral positions of the layered structure. This distance compares well with distances seen in other structures, such as Co_T−Co_O correlations (3.36 Å) in the spinel Co_3O_4,[45] the low-temperature (LT) form of $LiCoO_2$,[45,47] or gallium-substituted $LiNiO_2$.[49] Thus, treatment of LMNO with Li−Co−PO_4 leads to a complex integration of cobalt into the composite structure, rather than producing a $LiCoPO_4$ surface coating, with the cobalt ions located in both octahedral and tetrahedral sites of the LMNO host. As such, it appears that the reaction is somewhat similar to that which occurs for LNP-coated LCMO electrodes and that the incorporation of cobalt into the LMNO host is accompanied by the concomitant extrusion of lithium to produce Li_3PO_4, as evidenced by the XRD pattern in Figure 1(c)

The formation of $NiMn_6$ regions in the transition metal layers of LNP-treated LCMO suggests that the presence of locally clustered Li_2MnO_3:$LiCoO_2$ domain structures gives rise to an energetically favorable route for nickel insertion into the lithium sites of the transition metal layers that can be vacated during the Li−Ni−PO_4 acid-treatment 'leaching' process. Furthermore, such doping of the Li_2MnO_3-like regions with Ni^{2+} would add a small capacity enhancement to treated electrodes.

Interestingly, the Ni EXAFS data of an LCMO sample that had been treated with Li−Ni−PO_4 and subsequently heated at low temperature (∼100 °C), referred to as LCMO/LNP_LT), can be modeled using Ni−O and Ni−P correlations, whereas no acceptable fit to the data could be obtained using a layered α/β-$Ni(OH_2)$-type structure. Figure 8(a) shows the real part of the Fourier transformed Ni K-edge data (black) together with a fit of the first two shells (red). The Fourier transform magnitude, along with the fit, are shown in the inset. As reported in Table 1, the coordination numbers for the first-shell Ni−O and second-shell Ni−P are determined to be ∼6.0 and ∼4.0 with bond distances of ∼2.05 Å and ∼3.24 Å, respectively, which agree well with those expected for an olivine $LiNiPO_4$-type structure. However, for a well-crystallized $LiNiPO_4$ additional contributions from a Ni−P correlation at ∼2.73 Å and four Ni−Ni correlations at ∼3.78 Å are also expected in the olivine structure.[50] Clearly such interactions are not evident in the EXAFS of the LCMO/LNP_LT sample, suggesting the absence of well-crystallized $LiNiPO_4$. This inference is not surprising considering the low-temperature (∼100 °C) treatment used during this synthesis step. In addition, XRD of the LCMO/LNP_LT sample, shown in Figure 1(d), does not indicate the presence of Li_3PO_4. Therefore, there is no evidence for nickel association with either a crystalline $LiNiPO_4$ or Li_3PO_4-type phase at this point in the synthesis. That being said, the EXAFS data clearly reveal the presence of interactions involving nickel atoms with phosphate moieties. Interestingly, the ordering peaks, characteristic of the Li_2MnO_3 component just above ∼20° 2θ, have been washed out by the low-temperature treatment. This is also consistent with the Mn EXAFS for this sample (not shown) which reveals local and medium-range changes in the Mn environment. This observation gives some insight into the solution-phase chemistry of our synthesis and is consistent with the EXAFS showing that the Li_2MnO_3 component of the composite material is most affected by the Li−Ni−PO_4 sol−gel treatment. We therefore conclude that nickel migration into the transition metal layers occurs only on high-temperature annealing, as described above, the acidic phosphate solution being responsible for leaching lithium ions from the LCMO structure to enable Li_3PO_4 to precipitate at the particle surface. The introduction of divalent nickel for monovalent lithium in the structure must be associated with creation of vacancies and/or the reduction of Mn^{4+} to Mn^{3+} in the LCMO structure for charge balance. One caveat to the hypothesis of pure Li_3PO_4 formation at the particle surface is that Li_3PO_4-treated 'layered−layered' composite electrodes have a higher impedance (lower rate capability) than electrodes treated with Li−Ni−PO_4 compositions, suggesting that the nickel ions play a role in the surface stabilization of these electrodes.[23] The possibility of a defect $Li_{3-2x}Ni_xPO_4$ structure at the particle surface, on high-temperature annealing, has been proposed.[23]

Although we have demonstrated nickel migration into the Li_2MnO_3-like domains of $0.5Li_2MnO_3 \bullet 0.5LiCoO_2$ materials, it is evident from Figure 8(b) that our process does not result in the same cation arrangements found in Li−Mn−Ni−O composite structures when prepared by traditional synthesis methods. Specifically, Figure 8(b) shows a comparison of the Fourier transformed Ni K-edge data (3−13 $Å^{-1}$) of LNP-treated LCMO (point 1, Figure 3) with the Ni^{2+} reference, $0.5Li_2MnO_3 \bullet 0.5LiMn_{0.5}Ni_{0.5}O_2$, which was prepared by precipitation and subsequent annealing of metal hydroxides. Figure 8(c) shows the imaginary part of the transform that reveals an increasing phase mismatch with increasing R. These observations endorse the uniqueness of our method for synthesizing and tailoring, composite electrode materials and their surface structures.

The findings described above lead to the conclusion that metal cations can be substituted directly into Li_2MnO_3-based composite electrode structures under acidic conditions to modify the electrode composition, particularly at the surface. Furthermore, our XAS analyses imply that Li_2MnO_3, in the presence of other metal cations and under acidic conditions, may be able to serve as a precursor for the synthesis of high-capacity composite cathode materials. Such studies have already been undertaken by our group, which validates this concept;

the studies have also revealed that the technique is extremely simple and versatile and can be used to prepare a wide range of known and novel composite electrode structures.[24]

CONCLUSIONS

We have designed and conducted an experiment that capitalizes on the inherent, element-specific nature of XAS to elucidate the chemical and structural outcome of the surface treatments of layered, composite cathode materials $xLi_2MnO_3\bullet(1-x)LiMO_2$ (M = Mn, Ni, Co). A Li−Ni−PO_4 composition, chosen for its expected electrochemical stability at high potentials, was deposited by an acidic sol−gel method on the surface of $0.5Li_2MnO_3\bullet0.5LiCoO_2$. X-ray absorption data have revealed that the nickel ions do not exist in a phosphate environment after samples are annealed at 550 °C. Rather, it has been found, within the accuracy of the measurements, that the nickel ions replace the lithium ions in the transition metal layers of the Li_2MnO_3 component of the $0.5Li_2MnO_3\bullet0.5LiCoO_2$ structure, giving rise to fully coordinated $NiMn_6$ units within the composite structure, and yielding a Li_3PO_4-like byproduct, presumably at the electrode particle surface. The Ni^{2+} ions in the Li_2MnO_3-like regions are electrochemically active and therefore contribute to the working capacity of the electrode.

EXAFS data of $0.5Li_2MnO_3\bullet0.5LiMn_{0.5}Ni_{0.5}O_2$ ($Li_{1.2}Mn_{0.6}Ni_{0.2}O_2$) treated with Li−Co−$PO_4$ in a similar fashion also provide evidence that cobalt is accommodated within the transition metal layers of the host structure but not with the same degree of cation order as when nickel is substituted for lithium in $0.5Li_2MnO_3\bullet0.5LiCoO_2$. These results and our approach to use Li_2MnO_3 as a precursor in combination with electrochemically active transition metal ions in acidic solution have significant implications for synthesizing and tailoring high-capacity lithiated-metal-oxide electrode materials and their surface structures.

AUTHOR INFORMATION

Corresponding Author

*E-mail: mali@aps.anl.gov (M.B.), thackeray@anl.gov (M.M.T.).

ACKNOWLEDGMENTS

Financial support for J.R.C., D.K., and S.H.K. from the Office of Vehicle Technologies of the U.S. Department of Energy (DOE) is gratefully acknowledged. MMT was supported by the Center for Electrical Energy Storage: Tailored Interfaces, an Energy Frontier Research Center funded by the U.S. Department of Energy, Office of Science, Office of Basic Energy Sciences. M.B. and Sector 20 facilities at the Advanced Photon Source of Argonne National Laboratory, and research at these facilities, are supported by the U.S. DOE, Basic Energy Sciences, and National Sciences and Engineering Research Council of Canada and its founding institutions. Visualization and graphic representation of structures facilitated by Jmol: http://www.jmol.org/

. The submitted manuscript has been created by UChicago Argonne, LLC, Operator of Argonne National Laboratory ("Argonne"). Argonne, a U.S. Department of Energy Office of Science laboratory, is operated under Contract No. DE-AC02-06CH11357. The U.S. Government retains for itself, and others acting on its behalf, a paid-up, nonexclusive, irrevocable worldwide license in said article to reproduce, prepare derivative works, distribute copies to the public, and perform publicly and display publicly, by or on behalf of the Government.

REFERENCES

(1) Nazar, L. F.; Ellis, B. L.; Lee, K. T. *Chem. Mater.* **2010**, *22*, 691.
(2) Whittingham, M. S. *Chem. Rev.* **2004**, *104*, 4271.
(3) Chen, Z. H.; Qin, Y.; Amine, K.; Sun, Y. K. *J. Mater. Chem.* **2010**, *20*, 7606.
(4) Kang, B.; Ceder, G. *Nature* **2009**, *458*, 190.
(5) Zaghib, K.; Goodenough, J. B.; Mauger, A.; Julien, C. *J. Power Sources* **2009**, *194*, 1021.
(6) Wu, Y.; Murugan, A. V.; Manthiram, A. *J. Electrochem. Soc.* **2008**, *155*, A635.
(7) Appapillai, A. T.; Mansour, A. N.; Cho, J.; Shao-Horn, Y. *Chem. Mater.* **2007**, *19*, 5748.
(8) Shao-Horn, Y.; Lu, Y. C.; Mansour, A. N.; Yabuuchi, N. *Chem. Mater.* **2009**, *21*, 4408.
(9) West, W. C.; Soler, J.; Smart, M. C.; Ratnakumar, B. V.; Firdosy, S.; Ravi, V.; Anderson, M. S.; Hrbacek, J.; Lee, E. S.; Manthiram, A. *J. Electrochem. Soc.* **2011**, *158*, A883.
(10) Kang, S. H.; Kempgens, P.; Greenbaum, S.; Kropf, A. J.; Amine, K.; Thackeray, M. M. *J. Mater. Chem.* **2007**, *17*, 2069.
(11) Bareno, J.; Balasubramanian, M.; Kang, S. H.; Wen, J. G.; Lei, C. H.; Pol, S. V.; Petrov, I.; Abraham, D. P. *Chem. Mater.* **2011**, *23*, 2039.
(12) Balasubramanian, M.; McBreen, J.; Davidson, I. J.; Whitfield, P. S.; Kargina, I. *J. Electrochem. Soc.* **2002**, *149*, A176.
(13) Pan, C. J.; Lee, Y. J.; Ammundsen, B.; Grey, C. P. *Chem. Mater.* **2002**, *14*, 2289.
(14) Grey, C. P.; Breger, J.; Meng, Y. S.; Hinuma, Y.; Kumar, S.; Kang, K.; Shao-Horn, Y.; Ceder, G. *Chem. Mater.* **2006**, *18*, 4768.
(15) Meng, Y. S.; Ceder, G.; Grey, C. P.; Yoon, W. S.; Jiang, M.; Breger, J.; Shao-Horn, Y. *Chem. Mater.* **2005**, *17*, 2386.
(16) Balasubramanian, M.; Sun, X.; Yang, X. Q.; McBreen, J. *J. Electrochem. Soc.* **2000**, *147*, 2903.
(17) Van der Ven, A.; Ceder, G. *Electrochem. Commun.* **2004**, *6*, 1045.
(18) Kim, J. S.; Johnson, C. S.; Vaughey, J. T.; Thackeray, M. M.; Hackney, S. A. *Chem. Mater.* **2004**, *16*, 1996.
(19) Johnson, C. S.; Kim, J. S.; Lefief, C.; Li, N.; Vaughey, J. T.; Thackeray, M. M. *Electrochem. Commun.* **2004**, *6*, 1085.
(20) Lu, Z. H.; Dahn, J. R. *J. Electrochem. Soc.* **2002**, *149*, A815.
(21) Obrovac, M. N.; Dunlap, R. A.; Sanderson, R. J.; Dahn, J. R. *J. Electrochem. Soc.* **2001**, *148*, A576.
(22) Thackeray, M. M.; Kang, S. H.; Johnson, C. S.; Vaughey, J. T.; Benedek, R.; Hackney, S. A. *J. Mater. Chem.* **2007**, *17*, 3112.
(23) Kang, S.-H.; Thackeray, M. M. *Electrochem. Commun.* **2009**, *11*, 748.
(24) Croy, J. R.; Kang, S. H.; Balasubramanian, M.; Thackeray, M. M. *Electrochem. Commun.* **2011**, *13*, 1063.
(25) Kraft, S.; Stumpel, J.; Becker, P.; Kuetgens, U. *Rev. Sci. Instrum.* **1996**, *67*, 681.
(26) Ravel, B.; Newville, M. *J. Synchrotron Radiat.* **2005**, *12*, 537.
(27) Jin, B. S.; Ha, K. H.; Jeong, J. H.; Kim, H. S.; Doh, C. H.; Moon, S. I. *Phys. Scr.* **2010**, T139.
(28) Boulineau, A.; Croguennec, L.; Delmas, C.; Weill, F. *Chem. Mater.* **2009**, *21*, 4216.
(29) Popovic, L.; Manoun, B.; de Waal, D.; Nieuwoudt, M. K.; Comins, J. D. *J. Raman Spectrosc.* **2003**, *34*, 77.
(30) Yoon, W. S.; Balasubramanian, M.; Yang, X. Q.; Fu, Z. G.; Fischer, D. A.; McBreen, J. *J. Electrochem. Soc.* **2004**, *151*, A246.
(31) Park, Y. J.; Hong, Y. S.; Wu, X. G.; Kim, M. G.; Ryu, K. S.; Chang, S. H. *Bull. Korean Chem. Soc.* **2004**, *25*, 511.
(32) Arachi, Y.; Kobayashi, H.; Emura, S.; Nakata, Y.; Tanaka, M.; Asai, T. *Phys. Scr.* **2005**, *T115*, 577.
(33) Kim, M. G.; Shin, H. J.; Kim, J. H.; Park, S. H.; Sun, Y. K. *J. Electrochem. Soc.* **2005**, *152*, A1320.
(34) Yoon, W. S.; Balasubramanian, M.; Chung, K. Y.; Yang, X. Q.; McBreen, J.; Grey, C. P.; Fischer, D. A. *J. Am. Chem. Soc.* **2005**, *127*, 17479.
(35) Howard, W. F.; Spotnitz, R. M. *J. Power Sources* **2007**, *165*, 887.

(36) Reed, J.; Ceder, G. *Electrochem. Solid-State Lett.* **2002**, *5*, A145.
(37) Yoon, W. S.; Grey, C. P.; Balasubramanian, M.; Yang, X. Q.; McBreen, J. *Chem. Mater.* **2003**, *15*, 3161.
(38) Li, J. Y.; Jensen, T. B. S.; Andersen, N. H.; Zarestky, J. L.; McCallum, R. W.; Chung, J. H.; Lynn, J. W.; Vaknin, D. *Phys. Rev. B* **2009**, 79.
(39) Pickering, I. J.; George, G. N.; Lewandowski, J. T.; Jacobson, A. J. *J. Am. Chem. Soc.* **1993**, *115*, 4137.
(40) Mansour, A. N.; Croguennec, L.; Delmas, C. *Electrochem. Solid-State Lett.* **2005**, *8*, A544.
(41) Nakai, I.; Takahashi, K.; Shiraishi, Y.; Nakagome, T.; Izumi, F.; Ishii, Y.; Nishikawa, F.; Konishi, T. *J. Power Sources* **1997**, *68*, 536.
(42) Demourgues, A.; Gautier, L.; Chadwick, A. V.; Delmas, C. *Nucl. Instrum. Methods Phys. Res., Sect. B* **1997**, *133*, 39.
(43) Peres, J. P.; Demourgues, A.; Delmas, C. *Solid State Ionics* **1998**, *111*, 135.
(44) Koleva, V.; Zhecheva, E.; Stoyanova, R. *Eur. J. Inorg. Chem.* **2010**, 4091.
(45) Koyano, G.; Watanabe, H.; Okuhara, T.; Misono, M. *J. Chem. Soc., Faraday Trans.* **1996**, *92*, 3425.
(46) Yamamoto, T. *X-Ray Spectrom.* **2008**, *37*, 572.
(47) Gummow, R. J.; Thackeray, M. M.; David, W. I. F.; Hull, S. *Mater. Res. Bull.* **1992**, *27*, 327.
(48) Montoya, A.; Haynes, B. S. *Chem. Phys. Lett.* **2011**, *502*, 63.
(49) Balasubramanian, M.; McBreen, J.; Pandya, K.; Amine, K. *J. Electrochem. Soc.* **2002**, *149*, A1246.
(50) Abrahams, I.; Easson, K. S. *Acta Crystallogr., Sect. C: Cryst. Struct. Commun* **1993**, *49*, 925.